A micromechanically based model for strain rate effects in unidirectional composites

Mechanics of Materials 148 (2020) 103491

Contents lists available at ScienceDirect

Mechanics of Materials

journal homepage: www.elsevier.com/locate/mechmat

Research paper

A micromechanically based model for strain rate effects in unidirectional composites

Larsson R.*[,a], Singh V.[b,a], Olsson R.[b,a], Marklund E.[b]

[a] Division of Material and Computational Mechanics, Department of Industrial and Materials Science, Chalmers University of Technology, SE-412 96 Göteborg, Sweden
[b] Division of Materials and Production, RISE SICOMP, SE-431 22 Mölndal, Sweden

ARTICLE INFO

Keywords:
Strain rate dependence
Micromechanics
Unidirectional (UD) ply
Off-axis loading

ABSTRACT

This article addresses dynamic behaviour of fibre reinforced polymer composites in terms of a transversely isotropic viscoelastic-viscoplastic constitutive model established at the unidirectional ply level. The model captures the prelocalized response of the ply in terms of rate dependent elasticity and strength without damage. A major novelty is that the model draws from computational homogenization, with matrix and fibre materials as subscale constituents for a representative volume element of the ply. The micromechanics of the strain rate dependent polymer matrix is represented by an isotropic pressure sensitive viscoelastic-viscoplastic prototype model. For the fibre material, transverse elasticity is assumed. The constituents are homogenized via the fluctuating strain of the subscale, where a simple ansatz is applied to allow for constant stress in the plane transverse to the fibre orientation. Despite the relatively simple modelling assumptions for the constituents, the homogenized model compares favourably to experimental data for an epoxy/carbon fibre based composite, subjected to a variety of challenging uniaxial off-axis tests. The model response clearly reflects observed strain rate dependencies under both tensile and compressive loadings.

1. Introduction

Carbon Fibre Reinforced Polymer (CFRP) composites are increasingly used for lightweight design in transport applications. In aeronautics and in naval structures, CFRP composites have been used for several decades. Driven by the increasing demand to reduce the carbon emissions, CFRPs are being considered also in automotive. For combustion engines, the relation between fuel consumption and weight of the vehicle is direct, cf. Mårtensson (2016), whereas electrical vehicles benefit from light weight design by increased driving range or reduced need for electrical charging. Because of the extensive and important CAE tools in the design methodology, CFRP must be included in this methodology so that the material can be fully exploited via e.g. efficient and accurate Finite Element (FE) modelling tools. Due to the decisive design criteria induced from safety, the integration of fibre reinforced polymers in the CAE tools in the design process is of utmost importance to be able to carry out full FE-based crash analyses.

Typically, CFRP is used in components where superior stiffness, strength and energy absorption (in crushing) properties per unit weight of the material can be exploited, cf. refs Carruthers et al. (1998); Jacob et al. (2002). As to the crushing property of CFRPs, it depends strongly on the proper triggering of the failure modes, cf. e.g. Grauers et al. (2014). In order to complement the understanding of the inter- and intra-ply failure modes, there is an urgent need to include effects of strain rate in CFRP composites. Literature reviews of the relevant experimental work are given by e.g. Sierakowski (1997) and Singh (2018), where it is concluded that the dynamic response of fibre reinforced polymers is highly influenced by the loading rate. This is evidenced by the experimental works by Daniel and Liber (1976), Hsiao and Daniel (1998), Hosur et al. (2001), Yokoyama and Nakai (2009), Hsiao et al. (1999) and more recently for epoxy based CFRPs by Koerber et al., 2010; Ponte Castañeda, 1996. At the unidirectional (UD) ply level, the properties of the CFRP are strongly controlled by the polymer behaviour in shear, tension or compression transverse to the fibres and in compression along the fibres. It is only for quite small tensile off-axis loading that the UD composite becomes rate insensitive due to the strong fibre engagement. As to modelling, aspects of the pure polymer behavior have been treated extensively in the literature. In particular, epoxy under static loading typically exhibits elastoplastic behaviour with large failure strains ($>20\%$) in compression and shear, while the failure strain in tension is significantly lower ($<5\%$), implying that ultimate failure occurs before the fully plastic region has been reached, as demonstrated in e.g. Marklund et al. (2014); Fiedler et al. (2001). The failure strains of fibre

* Corresponding author.
E-mail addresses: ragnar.larsson@chalmers.se, ragnar@chalmers.se (R. Larsson).

https://doi.org/10.1016/j.mechmat.2020.103491
Received 2 January 2020; Received in revised form 20 May 2020; Accepted 22 May 2020
Available online 08 June 2020

reinforced polymer composites are significantly lower than in the pure polymer, particularly under tension, due to stress concentrations induced by the microstructural fibre/matrix morphology. However, literature on material modelling specifically addressing the influence of strain rate in fibre reinforced polymers is limited. We may mention the anisotropic elastic-viscoplastic models by Vogler et al. (2013), Koerber et al. (2018) and Gerbaud et al. (2019).

Micromechanical homogenisation plays an important part in composites modeling. Concepts for the homogenization have been developed by e.g. Hashin (1983) and Christensen and Lo (1979) considering the constituents as concentric circular cylinders. A commonly used micromechanical model was presented by Mori and Tanaka (1973), which gives quite accurate predictions for composites with aligned or randomly oriented reinforcements. Procedures for estimating the effective composite behaviour with nonlinear phase materials have been presented based on the linearized response, e.g. by Ponte Castañeda, 1996.

In the present paper, the dynamic behaviour of CFRP composites is addressed in terms of a transversely isotropic viscoelastic-viscoplastic constitutive model applied to a UD carbon-epoxy composite. We emphasize the prelocalized material response, focusing on the rate dependent stiffness and strength properties (without damage) in the material. As compared to the recent models in Koerber et al. (2018) and Gerbaud et al. (2019) directly addressing the anisotropic ply response, the present model draws from computational homogenization. The micromechanics of the model is established at the ply scale, where the matrix and fibre materials represent the subscale constituents. In contrast to homogenization techniques exploiting analytical solutions, the individual matrix and fibre constituents are connected via computational homogenization for a piece-wise constant strain field at the subscale. Here, the matrix material is represented by an isotropic pressure sensitive viscoelastic-viscoplastic prototype model to describe the strain rate dependent matrix response. In this paper, the pressure dependence relates to the onset of matrix shear yielding under compressive and tensile stress responses. The fibre constituent model is based on a structural tensor-based formulation along the lines set out in Larsson et al. (2018) for fibre compression/extension and shear. Based on the Hill-Mandel condition, cf. Hill (1963), Suquet (1985) and Miehe et al. (1999), the constituents are homogenized via the fluctuating strain of the subscale. To arrive at an efficient but still representative model, a simple ansatz is applied to the structure of the fluctuating strains leading to a non-standard homogenized response of the composite. The model is applied to the nonlinear rate dependent anisotropic ply behaviour under quasi-static and dynamic loadings at different off-axis angles. For the relatively simple viscoelastic-viscoplastic prototype for the matrix response, there is a good correlation between measured and model responses of the IM7/8552 carbon-epoxy composite in compression and tension, Koerber et al. (2010). The simplicity of the homogenization scheme contributes to computational efficiency of the model. The present formulation focuses on the nonlinear rate dependent anisotropic ply behaviour under quasi-static and dynamic loadings. Future development of the model will focus on prediction of failure after the onset of inelastic deformation and address the influence of rate dependent fibres.

The paper is organized as follows: Firstly, the constitutive model development framework is presented. The material model calibration is discussed and validated with experimental results. The dynamic response of pure resin from the proposed model is presented and discussed. Finally, the main conclusions of the work are made and future work is discussed.

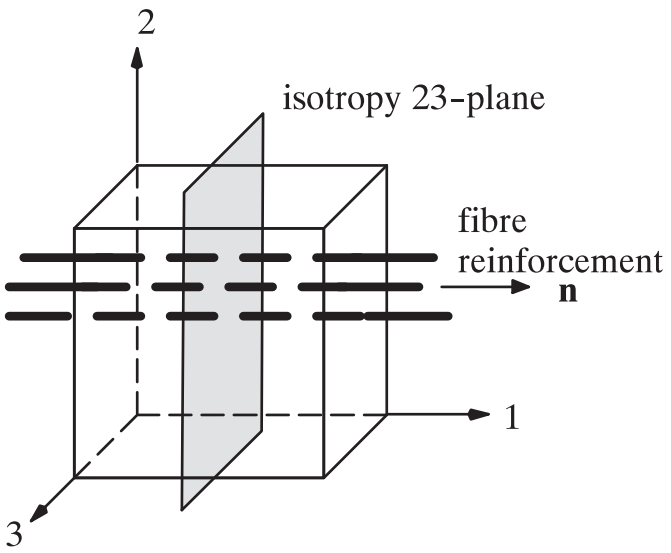

Fig. 1. A UD–ply composite in transverse isotropy with fibre orientation $\boldsymbol{n}$. From ref. Larsson et al. (2018).

2. A micromechanics based model for strain rate effects in UD ply composites

2.1. Strain representations

As a preliminary to the subsequent model development, a set of strain representations for the description of transverse material response are introduced in this section. In particular, a composite material comprising an *isotropic* polymer matrix with an embedded fibre is considered. The fibre material is considered elastic *transversely isotropic*, where the fibre orientation is described by the *unit* normal vector $\boldsymbol{n}$ as shown in Figure 1. To represent actions normal to the fibre face the structure tensor $\boldsymbol{m} = \boldsymbol{n} \otimes \boldsymbol{n}$ is used.

For the representation of isotropy, the engineering strain tensor $\boldsymbol{\epsilon}$ is subdivided into deviatoric and volumetric parts defined as

$$\boldsymbol{\epsilon} = \boldsymbol{\epsilon}_d + \frac{1}{3}\epsilon_{vol}\boldsymbol{1} \tag{1}$$

where $\boldsymbol{1}$ is the second order identity tensor. The deviatoric part is the projection $\boldsymbol{\epsilon}_d = \boldsymbol{I}_d : \boldsymbol{\epsilon}$ and the volumetric strain is $\epsilon_{vol} = \boldsymbol{1} : \boldsymbol{\epsilon}$, where the deviatoric fourth order projection tensor $\boldsymbol{I}_d$ is defined as

$$\boldsymbol{I}_d = \boldsymbol{I} - \frac{1}{3}\boldsymbol{1} \otimes \boldsymbol{1} \text{ with } \boldsymbol{I} = \boldsymbol{1} \bar{\otimes} \boldsymbol{1} \tag{2}$$

Here, the dyadic product $\boldsymbol{A} = \boldsymbol{a} \bar{\otimes} \boldsymbol{c}^t$ defines the fourth order tensor $\boldsymbol{A}$ in terms of the second order tensors $\boldsymbol{a}$ and $\boldsymbol{c}$. The symbol $\bar{\otimes}$ defines the double contraction $\boldsymbol{A} : \boldsymbol{b} = \boldsymbol{a} \cdot \boldsymbol{b} \cdot \boldsymbol{c}$, cf. Steinmann et al. Steinmann et al. (1997).

For the representation of elastic transverse isotropy of the fibre material, the longitudinal shear/axial fibre strain tensor $\boldsymbol{\epsilon}_{sa}$ is introduced in terms of its *pure* shear $\boldsymbol{\epsilon}_s$ and axial fibre strain ϵ_a counterparts written as

$$\boldsymbol{\epsilon}_{sa} = \boldsymbol{I}_{sa} : \boldsymbol{\epsilon} = (\boldsymbol{m} \cdot \boldsymbol{\epsilon})^{\text{sym}} = \boldsymbol{\epsilon}_s + \epsilon_a \boldsymbol{m} \tag{3}$$

where $\boldsymbol{\epsilon}_s = \boldsymbol{I}_s : \boldsymbol{\epsilon}$ and $\epsilon_a = \boldsymbol{m} : \boldsymbol{\epsilon}$. Here, $\boldsymbol{I}_s$ is the fourth order fibre shear projection tensor defined as

$$\boldsymbol{I}_s = \boldsymbol{I}_{sa} - \boldsymbol{m} \otimes \boldsymbol{m} \quad \text{with } \boldsymbol{I}_{sa} = \frac{1}{2}(\boldsymbol{m} \bar{\otimes} \boldsymbol{1} + \boldsymbol{1} \bar{\otimes} \boldsymbol{m}) \tag{4}$$

Here it may be noted that $\boldsymbol{I}_s : \boldsymbol{1} = \boldsymbol{I}_s : \boldsymbol{m} = \boldsymbol{0}$ and the pure fibre shear strain tensor can be obtained in the shear strain vector $\boldsymbol{\gamma} = \boldsymbol{\epsilon} \cdot \boldsymbol{n} - \epsilon_a \boldsymbol{n}$ as

$$\boldsymbol{\epsilon}_s = \frac{1}{2}(\boldsymbol{n} \otimes \boldsymbol{\gamma} + \boldsymbol{\gamma} \otimes \boldsymbol{n}) \tag{5}$$

Hence, upon introducing the longitudinal fibre shear strain as $\gamma = |\boldsymbol{\gamma}|$, cf. also Larsson et al. (2018), one obtains

$$\gamma^2 = 2\epsilon_s : \epsilon_s \tag{6}$$

Let us also introduce the strain tensor $\hat{\boldsymbol{\epsilon}}$ that is confined to the plane *transverse* to the UD fibres. This tensor is defined as a projection of the total strain onto the transverse fibre plane via the identity tensor of the transverse fibre plane $\hat{\boldsymbol{I}}$ written as

$$\hat{\boldsymbol{\epsilon}} = (\boldsymbol{\epsilon}\cdot\hat{\boldsymbol{I}})^{\text{sym}} = \hat{\boldsymbol{I}} : \boldsymbol{\epsilon} \;\text{ with }\; \hat{\boldsymbol{I}} = \frac{1}{2}(\hat{\boldsymbol{I}} \otimes \boldsymbol{1} + \boldsymbol{1} \otimes \hat{\boldsymbol{I}}) \tag{7}$$

where $\hat{\boldsymbol{I}} := \boldsymbol{1} - \boldsymbol{m}$ and $\hat{\boldsymbol{I}}$ is the 4th order transverse fibre plane projection operator. As to the definition of $\hat{\boldsymbol{I}}$, consider the displacement gradient $\hat{\boldsymbol{h}}$ of the isotropy plane with the property $\hat{\boldsymbol{h}} : \boldsymbol{m} = 0$. Hence, the superficial displacement gradient is confined to the isotropy plane so that

$$\hat{\boldsymbol{h}} = \boldsymbol{u}_{,\alpha} \otimes \boldsymbol{g}^{\alpha} = (\boldsymbol{u}_{,\alpha} \otimes \boldsymbol{g}^{\alpha})\cdot(\boldsymbol{g}_{\beta} \otimes \boldsymbol{g}^{\beta}) \tag{8}$$

Here, $\boldsymbol{g}^{\alpha}$ is the contra-variant basis vector of the isotropy plane, where the Greek indices α, β range over 2,3 as indicated in Figure 1. The corresponding co-variant basis vector $\boldsymbol{g}_{\alpha}$ is related to $\boldsymbol{g}^{\alpha}$ via $\hat{\boldsymbol{I}} := \boldsymbol{g}_{\beta} \otimes \boldsymbol{g}^{\beta} = \boldsymbol{1} - \boldsymbol{m}$, whereby it follows that

$$\hat{\boldsymbol{\epsilon}} = \hat{\boldsymbol{h}}^{\text{sym}} = (\boldsymbol{h}\cdot\hat{\boldsymbol{I}})^{\text{sym}} = (\boldsymbol{\epsilon}\cdot\hat{\boldsymbol{I}})^{\text{sym}} \tag{9}$$

2.2. Homogenized response of the polymer matrix-fibre composite

In order to homogenize the ply level matrix-fibre composite response, consider a Representative Volume Element (RVE) $B_{\square}$ of the polymer matrix-fibre composite in Figure 2. The polymer matrix material locates in the region $B^{\text{m}}_{\square}$ and the fibre material locates in the region $B^{\text{f}}_{\square}$. Consider also the microscopic strain field $\boldsymbol{\epsilon} \in B_{\square}$ additively split into a macroscopic, constant strain $\bar{\boldsymbol{\epsilon}} = (\bar{\boldsymbol{u}} \otimes \nabla)^{\text{sym}}$ in the RVE (where $\bar{\boldsymbol{u}}$ is the macroscopic displacement of the solid), and a fluctuating portion $\tilde{\boldsymbol{\epsilon}} \in B_{\square}$. The total strain in $B_{\square}$ is thus obtained as

$$\boldsymbol{\epsilon} = \bar{\boldsymbol{\epsilon}} + \tilde{\boldsymbol{\epsilon}} \tag{10}$$

In order to derive the homogenized response of the deformation process in the RVE, the principle of virtual work equivalence applied to the representative region $B_{\square}$ in Figure 2 is exploited, cf. e.g. the basic refs. Suquet (1985), Miehe et al. (1999). Hence, the virtual work produced in $B_{\square}$ is equated by the corresponding virtual work produced at the continuum macroscopic level formulated as

$$V_{\square}\delta\bar{\boldsymbol{\epsilon}} : \bar{\boldsymbol{\sigma}} = \int_{B^{\text{m}}_{\square}} \delta\tilde{\boldsymbol{\epsilon}} : \boldsymbol{\sigma} dB + \int_{B^{\text{f}}_{\square}} \delta\tilde{\boldsymbol{\epsilon}} : \boldsymbol{\sigma} dB + \int_{B_{\square}} \delta\tilde{\boldsymbol{\epsilon}} : \boldsymbol{\sigma} dB \tag{11}$$

where $V_{\square} = m[B_{\square}]$ (m is the measure of the region $B_{\square}$) is the volume of

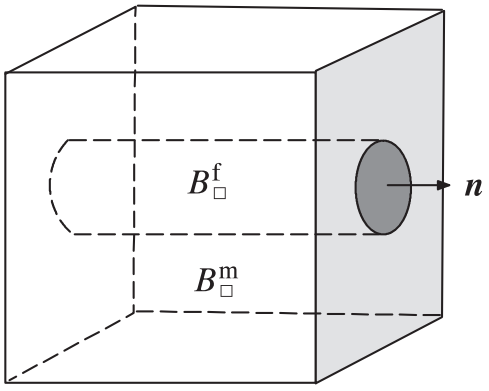

Fig. 2. Representative volume element of composite with volume $V_{\square}$ with a fibre region $B^{\text{f}}_{\square} \in B_{\square}$ (with the fibre orientation vector $\boldsymbol{n}$) embedded in the polymer matrix $B^{\text{m}}_{\square} \in B_{\square}$.

the RVE and the virtual work is split into the polymer matrix region $B^{\text{m}}_{\square} \subset B_{\square}$ and the fibre region $B^{\text{f}}_{\square} \subset B_{\square}$. Since $\delta\bar{\boldsymbol{\epsilon}}$ is constant in $B_{\square}$, eq. (11) can be rewritten as

$$\delta\bar{\boldsymbol{\epsilon}} : \bar{\boldsymbol{\sigma}} = \delta\bar{\boldsymbol{\epsilon}} : ((1 - v^{\text{f}})\boldsymbol{\sigma}^{\text{m}} + v^{\text{f}}\boldsymbol{\sigma}^{\text{f}}) + \frac{1}{V_{\square}} \int_{B_{\square}} \delta\tilde{\boldsymbol{\epsilon}} : \boldsymbol{\sigma} dB \tag{12}$$

where $v^{\text{f}} = V^{\text{f}}_{\square}/V_{\square}$ is the fibre volume content. The intrinsic homogenized polymer matrix and fibre stresses $\boldsymbol{\sigma}^{\text{m}}$, $\boldsymbol{\sigma}^{\text{f}}$ are defined as the volumetric means within the matrix and fibre regions written as

$$\boldsymbol{\sigma}^{\text{m}} := \frac{1}{V^{\text{m}}_{\square}} \int_{B^{\text{m}}_{\square}} \boldsymbol{\sigma} dB \quad , \quad \boldsymbol{\sigma}^{\text{f}} := \frac{1}{V^{\text{f}}_{\square}} \int_{B^{\text{f}}_{\square}} \boldsymbol{\sigma} dB \tag{13}$$

In addition to the virtual work equivalence in (11), the kinematic compatibility condition for the fluctuating strain field states that the volumetric mean of the fluctuating strain field is zero, i.e.

$$\frac{1}{V_{\square}} \int_{B_{\square}} \bar{\boldsymbol{\sigma}} : \tilde{\boldsymbol{\epsilon}} dB = \frac{1}{V_{\square}} \bar{\boldsymbol{\sigma}} : \int_{B_{\square}} \tilde{\boldsymbol{\epsilon}} dB = 0 \tag{14}$$

In order to arrive at a simplistic but yet still representative homogenized response of the composite, the following assumptions are made:

1. it is assumed that spatially *constant strain in the fibre direction* is acceptable, even in the nonlinear regime of the micromechanical response.
2. it is assumed that spatially *constant stress in the transverse fibre plane* is acceptable, compensated by a strain fluctuation $\tilde{\boldsymbol{\epsilon}}$ that is active solely in the transverse fibre plane.

Hence, from these assumptions, the stress and strain fields are *piecewise constant* in $B_{\square}$ so that

$$\tilde{\boldsymbol{\epsilon}} = \begin{cases} \tilde{\boldsymbol{\epsilon}}^{\text{m}} & \boldsymbol{x} \in B^{\text{m}}_{\square} \\ \tilde{\boldsymbol{\epsilon}}^{\text{f}} & \boldsymbol{x} \in B^{\text{f}}_{\square} \end{cases}, \; \boldsymbol{\sigma} = \begin{cases} \boldsymbol{\sigma}^{\text{m}}[\boldsymbol{\epsilon}] & \boldsymbol{x} \in B^{\text{m}}_{\square} \\ \boldsymbol{\sigma}^{\text{f}}[\boldsymbol{\epsilon}] & \boldsymbol{x} \in B^{\text{f}}_{\square} \end{cases} \tag{15}$$

whereby the virtual work equivalence (12) may be specialized as

$$\delta\bar{\boldsymbol{\epsilon}} : \bar{\boldsymbol{\sigma}} = \delta\bar{\boldsymbol{\epsilon}} : ((1 - v^{\text{f}})\boldsymbol{\sigma}^{\text{m}} + v^{\text{f}}\boldsymbol{\sigma}^{\text{f}}) + (1 - v^{\text{f}})\delta\tilde{\boldsymbol{\epsilon}}^{\text{m}} : \boldsymbol{\sigma}^{\text{m}} + v^{\text{f}}\delta\tilde{\boldsymbol{\epsilon}}^{\text{f}} : \boldsymbol{\sigma}^{\text{f}} \tag{16}$$

From the kinematic condition (14) we have

$$\frac{1}{V_{\square}} \int_{B_{\square}} \tilde{\boldsymbol{\epsilon}} dB = \frac{1}{V_{\square}} \int_{B^{\text{m}}_{\square}} \tilde{\boldsymbol{\epsilon}}^{\text{m}} dB + \frac{1}{V_{\square}} \int_{B^{\text{f}}_{\square}} \tilde{\boldsymbol{\epsilon}}^{\text{f}} dB = (1 - v^{\text{f}})\tilde{\boldsymbol{\epsilon}}^{\text{m}} + v^{\text{f}}\tilde{\boldsymbol{\epsilon}}^{\text{f}} = 0 \tag{17}$$

leading to

$$\tilde{\boldsymbol{\epsilon}}^{\text{f}} = -\frac{1 - v^{\text{f}}}{v^{\text{f}}} \tilde{\boldsymbol{\epsilon}}^{\text{m}} \tag{18}$$

Combining (18) with (16) yields

$$\delta\bar{\boldsymbol{\epsilon}} : \bar{\boldsymbol{\sigma}} = \delta\bar{\boldsymbol{\epsilon}} : ((1 - v^{\text{f}})\boldsymbol{\sigma}^{\text{m}} + v^{\text{f}}\boldsymbol{\sigma}^{\text{f}}) + (1 - v^{\text{f}})\delta\tilde{\boldsymbol{\epsilon}}^{\text{m}} : (\boldsymbol{\sigma}^{\text{m}} - \boldsymbol{\sigma}^{\text{f}}) \tag{19}$$

In the application to the polymer matrix-fibre microstructure, we choose

$$\tilde{\boldsymbol{\epsilon}}^{\text{m}} := \alpha\, \hat{\boldsymbol{\epsilon}} \tag{20}$$

where α is (scalar) variable of the strain fluctuation and $\hat{\boldsymbol{\epsilon}}$ is the projected *macroscopic* strain tensor onto the transverse plane of the fibre. This superficial strain tensor is defined in terms of a 4th order fibre transverse projection of the macroscopic strain (7) written as

$$\hat{\boldsymbol{\epsilon}} = \hat{\boldsymbol{I}} : \bar{\boldsymbol{\epsilon}} \tag{21}$$

Moreover, since "δ" means the change in the strain field with respect to an infinitesimal change in the displacement parameters, we obtain the virtual strain $\delta\tilde{\boldsymbol{\epsilon}}^{\text{m}}$ as

$$\delta\tilde{\boldsymbol{\epsilon}}^{\text{m}} = \delta\alpha\hat{\boldsymbol{I}} : \bar{\boldsymbol{\epsilon}} + \alpha\hat{\boldsymbol{I}} : \delta\bar{\boldsymbol{\epsilon}} \tag{22}$$

Upon inserting (22) into (19), the virtual work equivalence relationship extends to

$$\bar{\boldsymbol{\sigma}}\colon \delta\bar{\boldsymbol{\varepsilon}} = ((1-v^{\mathrm{f}})\boldsymbol{\sigma}^{\mathrm{m}} + v^{\mathrm{f}}\boldsymbol{\sigma}^{\mathrm{f}} + \alpha(1-v^{\mathrm{f}})(\boldsymbol{\sigma}^{\mathrm{m}} - \boldsymbol{\sigma}^{\mathrm{f}})\colon \hat{\boldsymbol{I}})\colon \delta\bar{\boldsymbol{\varepsilon}} + \delta\alpha(1-v^{\mathrm{f}})(\boldsymbol{\sigma}^{\mathrm{m}} - \boldsymbol{\sigma}^{\mathrm{f}})\colon \hat{\boldsymbol{I}}\colon \bar{\boldsymbol{\varepsilon}} \tag{23}$$

whereby the consistent homogenized macroscopic stress is obtained as

$$\bar{\boldsymbol{\sigma}} = ((1-v^{\mathrm{f}})\boldsymbol{\sigma}^{\mathrm{m}} + v^{\mathrm{f}}\boldsymbol{\sigma}^{\mathrm{f}})\colon (\boldsymbol{I} + \alpha\hat{\boldsymbol{I}}) - \alpha\boldsymbol{\sigma}^{\mathrm{f}}\colon \hat{\boldsymbol{I}} \tag{24}$$

corresponding to the equilibrium condition

$$\delta\alpha(1-v^{\mathrm{f}})(\boldsymbol{\sigma}^{\mathrm{m}} - \boldsymbol{\sigma}^{\mathrm{f}})\colon \hat{\boldsymbol{\varepsilon}} = 0 \tag{25}$$

Evidently, the intrinsic matrix and fibre stresses balance each other in the transverse fibre plane via the projection $\boldsymbol{\sigma}^{\mathrm{m}}\colon \hat{\boldsymbol{\varepsilon}} = \boldsymbol{\sigma}^{\mathrm{f}}\colon \hat{\boldsymbol{\varepsilon}}$. For a given macroscopic strain $\hat{\boldsymbol{\varepsilon}}$, the condition (25) determines the strain fluctuation in terms the scalar α in (20) and the constitutive response of the matrix stress $\boldsymbol{\sigma}^{\mathrm{m}}[\boldsymbol{\varepsilon}]$ and the fibre stress $\boldsymbol{\sigma}^{\mathrm{f}}[\boldsymbol{\varepsilon}]$. The homogenized (effective) ply response is given by (24).

2.3. Material modelling of the polymer matrix and fibre constituents

In this section the modelling of the constituents is described. The nonlinear response of the polymer matrix is considered to be isotropic, where the strain rate dependence is viscoelastic-viscoplastic. The carbon fibre material is elastic with transverse isotropy, formulated in terms of the kinematics outlined in section 2.1.

2.3.1. Viscoelastic-viscoplastic model of the polymer matrix

In order to model the rate sensitive inelastic polymer matrix response, it is assumed that the "elastic" shear behaviour is linearly viscoelastic combined with a viscoplastic deformation mechanism describing the rate sensitive failure stress. The rheological model in Figure 3 allows us to consider the adopted viscoelastic-viscoplastic coupling. As shown in the figure, the coupling is described by the long term (equilibrated) shear modulus G_1 and the (instant) dynamic shear modulus $G_0 = G_1 + G_2$, representing the elastic response at very high loading rates (when the viscoelastic damper has no time to develop viscous deformation). Here, the G_2 parameter represents the difference between the dynamic and long term shear moduli. As to viscoplasticity, the viscoplastic damper starts to develop inelastic deformation as soon as the slider starts to open as defined in terms of an over-stress function, cf. Figure 3. In Figure 3 it was tacitly assumed that the isothermal condition prevails. However, for very high strain rates significant adiabatic temperature generation may occur, eventually causing thermal softening of the polymer, cf. ref. Siviour and Jordan (2016).

To model the polymer matrix, the stored free energy ψ^{m} (per unit volume of matrix material in $B^{\mathrm{m}}_{[\cdot]}$) is defined by the strain energy contributions

$$\psi^{\mathrm{m}} = \psi^{\mathrm{m}}_{d1} + \psi^{\mathrm{m}}_{d2} + \psi^{\mathrm{m}}_{vol} \tag{26}$$

representing the deviatoric (or shape distortion) energy (in ψ^{m}_{d1} and ψ^{m}_{d2}) and the volume change energy ψ^{m}_{vol}. The contribution ψ^{m}_{d1} defines the shear energy due to straining in the upper G_1-spring and ψ^{m}_{d2} determines strain energy stored in the G_2-spring. The explicit expressions and dependencies in these energies are thus formulated as

$$\psi^{\mathrm{m}}_{d1} = \frac{1}{2}2G_1|\boldsymbol{\varepsilon}^e_d|^2, \quad \psi^{\mathrm{m}}_{d2} = \frac{1}{2}2G_2|\boldsymbol{\varepsilon}^e_d - \boldsymbol{\varepsilon}^v_d|^2, \quad \psi^{\mathrm{m}}_{vol} = \frac{1}{2}K(\varepsilon_{vol})^2 \tag{27}$$

where K is the bulk modulus of the polymer representing the elastic stiffness in ψ^{m}_{vol}. Moreover, $\boldsymbol{\varepsilon}^v_d$ is the deviatoric (inelastic) viscous portion of the strain. The viscoplastic strain $\boldsymbol{\varepsilon}^p_d$ is involved in the elastic deviatoric strain, defined by $\boldsymbol{\varepsilon}^e_d = \boldsymbol{\varepsilon}_d - \boldsymbol{\varepsilon}^p_d$, representing the straining in ψ^{m}_{d1}, whereas $\boldsymbol{\varepsilon}^e_d - \boldsymbol{\varepsilon}^v_d$ is the elastic strain in the strain energy ψ^{m}_{d2}.

From the basic postulate that the mechanical dissipation rate $\mathcal{D}^{\mathrm{m}}$ of the polymer matrix is positive we have that

$$\mathcal{D}^{\mathrm{m}} \colon = \boldsymbol{\sigma}^{\boldsymbol{m}}\colon \dot{\boldsymbol{\varepsilon}} - \dot{\psi}^{\mathrm{m}} = \underbrace{(\boldsymbol{\sigma}^{\mathrm{m}}_{d1} + \boldsymbol{\sigma}^{\mathrm{m}}_{d2})}_{\boldsymbol{\sigma}^{\mathrm{m}}_d}\colon \dot{\boldsymbol{\varepsilon}}^p_d + \boldsymbol{\sigma}^{\mathrm{m}}_{d2}\colon \dot{\boldsymbol{\varepsilon}}^v_d \geq 0 \tag{28}$$

This corresponds to the total matrix stress $\boldsymbol{\sigma}^{\mathrm{m}} = \boldsymbol{\sigma}^{\mathrm{m}}_{d1} + \boldsymbol{\sigma}^{\mathrm{m}}_{d2} + \sigma^{\mathrm{m}}_m \boldsymbol{1}$, where the constitutive state equations are

$$\boldsymbol{\sigma}^{\mathrm{m}}_{d1} = \frac{\partial \psi^{\mathrm{m}}_{d1}}{\partial \boldsymbol{\varepsilon}^e_d} = 2G_1(\boldsymbol{\varepsilon}_d - \boldsymbol{\varepsilon}^p_d) \tag{29a}$$

$$\boldsymbol{\sigma}^{\mathrm{m}}_{d2} = \frac{\partial \psi^{\mathrm{m}}_{d2}}{\partial \boldsymbol{\varepsilon}^e_d} = 2G_2(\boldsymbol{\varepsilon}_d - \boldsymbol{\varepsilon}^p_d - \boldsymbol{\varepsilon}^v_d) \tag{29b}$$

$$\sigma^{\mathrm{m}}_m = \frac{\partial \psi^{\mathrm{m}}_{vol}}{\partial \varepsilon_{vol}} = K\varepsilon_{vol} \tag{29c}$$

We also find that the total deviatoric stress $\boldsymbol{\sigma}^{\mathrm{m}}_d \colon = \boldsymbol{\sigma}^{\mathrm{m}}_{d1} + \boldsymbol{\sigma}^{\mathrm{m}}_{d2}$ is obtained as

$$\boldsymbol{\sigma}^{\mathrm{m}}_d = 2G_0(\boldsymbol{\varepsilon}_d - \boldsymbol{\varepsilon}^p_d) - 2G_2\boldsymbol{\varepsilon}^v_d \tag{30}$$

Guided by the dissipation inequality (28), we introduce the non-associated viscoplastic evolution rule and the viscoelastic evolution rule related to the matrix shear behaviour defined as

$$\dot{\boldsymbol{\varepsilon}}^p_d = \lambda\frac{\partial \phi^*}{\partial \boldsymbol{\sigma}^{\mathrm{m}}_d} = \lambda \boldsymbol{f} \quad \text{with } \boldsymbol{f} = \frac{\partial \phi^*}{\partial \boldsymbol{\sigma}^{\mathrm{m}}_d} = \frac{3}{2}\frac{\boldsymbol{\sigma}^{\mathrm{m}}_d}{\sigma^e_d} \tag{31a}$$

$$\dot{\boldsymbol{\varepsilon}}^v_d = \frac{1}{2G_2 t_{2*}}\boldsymbol{\sigma}^{\mathrm{m}}_{d2} \tag{31b}$$

where the yield and plastic potential functions ϕ and ϕ^* are introduced as

$$\phi = \sigma^e_d - (c_y + \gamma p), \quad \phi^* = \sigma^e_d - c_y \tag{32}$$

Here, $\sigma^e_d = \sqrt{3/2}|\boldsymbol{\sigma}^{\mathrm{m}}_d|$ is the von Mises stress of the matrix, $p = -\sigma^{\mathrm{m}}_m$ is the matrix pressure. Moreover, c_y is the cohesive yield stress parameter, γ is the friction parameter in the yield function, t_{2^*} is the relaxation time parameter of the elastic viscous damper. Pertinent to uniaxial tests of the polymer, these parameters are obtained at yielding for a tensile test with the yield stress σ_t and compressive test with the yield stress $\sigma_c \geq \sigma_t$

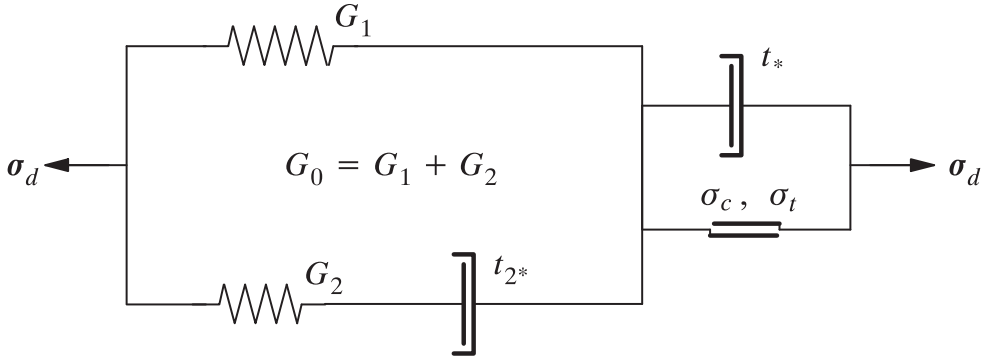

Fig. 3. Rheological model for the viscoelastic-viscoplastic response of the polymer matrix of the composite. It consists of a viscoelastic 3 parameter response combined with a viscoplastic deformation mechanism.

as

$$c_y = \frac{2}{1+\frac{\sigma_t}{\sigma_c}}\sigma_t, \quad \gamma = 3\frac{\sigma_c-\sigma_t}{\sigma_c+\sigma_t} \tag{33}$$

To describe the viscoplastic creep response in (31a), a Bingham creep model is employed in terms of the viscoplastic multiplier λ and the yield function ϕ defined as:

$$\lambda = \frac{1}{t_*}\eta[\phi] \geq 0 \text{ with } \eta[\phi]: = \frac{<\sigma_d^e - (c_y+\gamma p)>}{3G_0} \tag{34}$$

where t_* is the viscoplastic relaxation time and η is the overstress function. Indeed the inelastic response yields purely dissipative response, i.e.

$$\mathcal{D} = \boldsymbol{\sigma}_d^{\mathrm{m}}: \dot{\boldsymbol{\epsilon}}_d^p + \boldsymbol{\sigma}_{d2}^{\mathrm{m}}: \dot{\boldsymbol{\epsilon}}_d^v = \frac{1}{t_*}\eta[\phi]\sigma_d^e + \frac{1}{t_{2*}}\frac{(\sigma_{d2}^e)^2}{2G_2} \geq 0 \tag{35}$$

2.3.2. Transverse elastic modelling of the carbon fibre

The carbon fibre material of the UD-composite is assumed elastic with transverse isotropy. For this, the free energy ψ^{f} per unit volume of fibre material in $B_{\square}^{\mathrm{f}}$ is subdivided into four different elastic strain energy portions written as

$$\psi^{\mathrm{f}} = \psi_d^{\mathrm{f}} + \psi_{vol}^{\mathrm{f}} + \psi_s^{\mathrm{f}} + \psi_a^{\mathrm{f}} \tag{36}$$

The isotropic stored free energy contribution for the carbon fibre material consists of $\psi_d^{\mathrm{f}} + \psi_{vol}^{\mathrm{f}}$ defined as

$$\psi_d^{\mathrm{f}} = \frac{1}{2}2G^{\mathrm{f}}|\boldsymbol{\epsilon}_d|^2, \quad \psi_{vol}^{\mathrm{f}} = \frac{1}{2}K^{\mathrm{f}}(\epsilon_{vol})^2 \tag{37}$$

where G^{f} is the shear modulus of the fibre and K^{f} is the bulk modulus of the fibre. The anisotropic part of the stored free fibre energy consists of the longitudinal fibre shear part ψ_s and the part ψ_a due to axial straining along the fibres. In view of (6), the stored free shear fibre energy is defined as

$$\psi_s^{\mathrm{f}} = \frac{1}{2}G_s^{\mathrm{f}}\gamma^2 = \frac{1}{2}2G_s^{\mathrm{f}}|\boldsymbol{\epsilon}_s|^2 \tag{38}$$

and due to axial fibre straining, cf. Larsson et al. (2018), we consider

$$\psi_a^{\mathrm{f}} = \frac{1}{2}(1+\nu^{\mathrm{f}})E^{\mathrm{f}}\epsilon^2 = \frac{1}{2}(1+\nu^{\mathrm{f}})\frac{(\sigma^{\mathrm{f}})^2}{E^{\mathrm{f}}} \tag{39}$$

Here, E^{f} is the longitudinal fibre modulus of elasticity, σ^{f} is the uniaxial stress of the fibre, and ν^{f} is Poisson's ratio of the multiaxial response of the fibre in its longitudinal direction. Moreover, in (39) $\epsilon: = \sigma^{\mathrm{f}}/E^{\mathrm{f}}$ is the *uniaxial* fibre strain. It is related to the (kinematic) axial fibre strain $\epsilon_a = \boldsymbol{m}: \boldsymbol{\epsilon}$ via the uniaxial fibre response and a Poisson effect from the confinement fibre stress $\sigma_{\perp}^{\mathrm{f}}$, acting in the transverse plane to the fibre direction. Upon considering the fibre response multiaxial, standard application of Hooke's generalized law in the fibre direction yields

$$\epsilon_a = \frac{\sigma^{\mathrm{f}}}{E^{\mathrm{f}}} - \frac{\nu^{\mathrm{f}}}{E^{\mathrm{f}}}\sigma_{\perp}^{\mathrm{f}} \tag{40}$$

where E^{f} is the longitudinal fibre modulus of elasticity and ν^{f} is Poisson's ratio due to action in the fibre direction. In view of Figure 1, the confinement stress is $\sigma_{\perp}^{\mathrm{f}}: = \sigma_2^{\mathrm{f}} + \sigma_3^{\mathrm{f}} = \boldsymbol{1}: \boldsymbol{\sigma}^{\mathrm{f}} - \sigma^{\mathrm{f}}$ which may be described by

$$\sigma_{\perp}^{\mathrm{f}} = \frac{E^{\mathrm{f}}}{1-2\nu^{\mathrm{f}}}\epsilon_{vol} - \sigma^{\mathrm{f}} \tag{41}$$

The relations (40) and (41) are combined to yield the uniaxial strain as

$$\sigma^{\mathrm{f}} = E^{\mathrm{f}}\frac{(1-2\nu^{\mathrm{f}})\epsilon_a + \nu^{\mathrm{f}}\epsilon_{vol}}{(1-2\nu^{\mathrm{f}})(1+\nu^{\mathrm{f}})} \Rightarrow \epsilon = \frac{\sigma^{\mathrm{f}}}{E^{\mathrm{f}}} = \frac{(1-2\nu^{\mathrm{f}})\epsilon_a + \nu^{\mathrm{f}}\epsilon_{vol}}{(1-2\nu^{\mathrm{f}})(1+\nu^{\mathrm{f}})} \tag{42}$$

Since the fibre material is assumed elastic indeed $\mathcal{D}^{\mathrm{f}}: = 0$, corresponding to the total (intrinsic) fibre stress response $\boldsymbol{\sigma}^{\mathrm{f}} = \boldsymbol{\sigma}_d^{\mathrm{f}} + \boldsymbol{\sigma}_s^{\mathrm{f}} + \sigma_m^{\mathrm{f}}\boldsymbol{1} + \sigma_a^{\mathrm{f}}\boldsymbol{m}$. The individual stress contributions are thus obtained as

$$\boldsymbol{\sigma}_d^{\mathrm{f}} = \frac{\partial\psi_d^{\mathrm{f}}}{\partial\boldsymbol{\epsilon}_d} = 2G^{\mathrm{f}}\boldsymbol{\epsilon}_d \tag{43a}$$

$$\boldsymbol{\sigma}_s^{\mathrm{f}} = \frac{\partial\psi_s^{\mathrm{f}}}{\partial\boldsymbol{\epsilon}_s} = 2G_s^{\mathrm{f}}\boldsymbol{\epsilon}_s \tag{43b}$$

$$\sigma_m^{\mathrm{f}} = K^{\mathrm{f}}\epsilon_{vol} + \frac{\nu^{\mathrm{f}}}{1-2\nu^{\mathrm{f}}}E^{\mathrm{f}}\epsilon \tag{43c}$$

$$\sigma_a^{\mathrm{f}} = \frac{1}{1+\nu^{\mathrm{f}}}\frac{\partial\psi_a^{\mathrm{f}}}{\partial\epsilon} = E^{\mathrm{f}}\epsilon \tag{43d}$$

In order to establish the relation between the elastic fibre parameters of the tensor based formulation and the classical representation of a UD-ply, we follow the link to the classical elasticity representation of a UD-ply as formulated in Larsson et al. (2018). Here, the classical parameters E_L, E_T, G_{LT} and ν_{LT}, ν_{TT} are linked to the current five elastic parameters K^{f}, G^{f}, G_s^{f}, E^{f} and ν^{f} in a one to one mapping.

3. Calibration and validation of the constitutive model

3.1. Numerical implementation

The model has been implemented in a set of FORTRAN subroutines providing the uniaxial (compressive or tensile) response based on the general 3D formulation. In order to integrate the viscoelastic-viscoplastic flow rules the backward Euler method is used. It turns out that the well known "radial return property" for the integrated stress solution is retained in the present formulation, whereby an explicit stress update is obtained for a given strain increment. Some details of the integrated flow rule are given in the Appendix. In order to solve the local micromechanical problem (25) a Newton procedure was adopted, also contributing to the efficiency of the implementation. A gate to the MATLAB environment was implemented in order to handle mixed control (for the considered uniaxial tests) and to facilitate optimization of the material parameters.

3.2. Material selection and properties

To demonstrate the capabilities of the proposed viscoelastic-viscoplastic material model for capturing the rate dependent behaviour with composite laminates, the UD carbon/epoxy prepreg system IM7/8552 is considered. The experimental study for off-axis loadings of these UD laminates was performed by Koerber et al. (2010) for compressive loading and Kuhn et al. (2015) for tensile loading. The experiments consider the mechanical response at various strain rates and the fibre off-axis angles as shown in the Table 1, only the tensile testing does not include the 75° off-axis specimen. For the high strain rate testing a split-Hopkinson bar test machine was used in tension and in compression.

The elastic fibre properties used in the simulations are shown in

Table 1
List of fibre off-axis specimens and corresponding experimental axial strain rates in compression and tension. From refs. Koerber et al. (2010); Kuhn et al. (2015). No experimental data available for entries in brackets (indicated with #).

	Strain rates in compression [/s]		Strain rates in tension [/s]	
Fibre angle θ	Quasi - static	Dynamic	Quasi - static	Dynamic
15°	4×10^{-4}	122	2.1×10^{-4}	113
30°	4×10^{-4}	246	2.9×10^{-4}	177
45°	4×10^{-4}	321	2.6×10^{-4}	300
75°	4×10^{-4}	317	$(2.6\times10^{-4})^{\#}$	$(300)^{\#}$
90°	4×10^{-4}	276	2.8×10^{-4}	271

Table 2
Material parameters for transverse elasticity representing the carbon fibre.

E_L^f	E_T^f	G_{LT}^f	G_{TT}^f	K_{vol}^f	ν_{LT}^f	ν_{TT}^f	v^f
GPa	GPa	GPa	GPa	GPa	-	-	%
276	27	30	9.0	24.6	0.25	0.5	57

Table 3
Material parameters for the elastic isotropy of the epoxy material at quasi-static loading.

E^m	ν^m	$G_1 = G^m$	K^m
GPa	-	GPa	GPa
4.67	0.37	1.70	5.98

Table 2. The longitudinal modulus is according to the manufacturers data Hexcel Corporation, 2020, and the rest of the fibre properties are estimated based on typical values seen for HS and IM carbon fibres. These properties are necessary to calculate elastic fibre parameters of the tensor based formulation as stated in sub-section 2.3.2. The conversion between the classical elasticity parameters and the elasticity parameters for elastic transverse isotropy adopted in this paper is given in ref. Larsson et al. (2018). In addition the fiber volume fraction is $v^f = 57\%$, cf. also Table 2. The adopted properties for elastic isotropy of the epoxy 8552 resin (shown in Table 3) are obtained from refs. Hexcel Corporation, 2020 and Van Ee and Poursartip, 2009.

3.3. Model calibration

Even though the model is micromechanical, the individual phases are represented by phenomenological models. In the present application the model parameters assume fixed values, but they generally also depend on temperature and/or on other environmental factors. This subsection summarizes the main steps of the model parameter calibration against experimental uniaxial compressive and tensile tests. Subsequently, the calibrated model will be used for predicting the viscoelastic-viscoplastic response of the polymer composite under different loading rates.

In order to calibrate the material parameters, the 45° off-axis specimen of IM7/8552 Koerber et al. (2010) and Kuhn et al. (2015) is considered with respect to uniaxial tension and compression tests. Both quasi-static and dynamic experimental stress-strain responses are included in the calibration. As shown in Figure 3, the model generally involves six parameters to model the nonlinear viscoelastic-viscoplastic polymer matrix material formulated in sub-section 2.3.1. Three parameters are used to define viscous behaviour of the polymer matrix material: The long term and dynamic shear moduli, G_1, G_0 (via G_2) and the relaxation time t_{2*} associated with the viscoelastic response, and three other parameters pertaining to the viscoplastic response. These parameters are: σ_t, σ_c and t_* defining the quasi-static yield stress of the polymer matrix in tension and compression and the relaxation time associated with the viscoplastic response, respectively. Three of these parameters are known a priori, G_1, σ_t and σ_c, whereby the total number of parameters for calibration is reduced to three. In particular, the parameters σ_t and σ_c define the pressure dependence for yielding in the polymer matrix material.

For the calibration, a least square fit was made with respect to both the tensile and the compressive experimental data, which considers quasi-static and dynamic loading rates. In tension the loading rates are $\dot{\epsilon} = 2.6 \times 10^{-4}$ /s in quasi-static loading and $\dot{\epsilon} = 300$ /s in dynamic loading. In compression the loading rates are $\dot{\epsilon} = 4 \times 10^{-4}$ /s in quasi-static loading and $\dot{\epsilon} = 321$ /s in dynamic loading. The resulting calibrated model parameters are listed in Table 4.

Figure 4 shows the calibrated model and experimental responses for the 45° off-axis tests. The dashed blue and yellow curves refer to the quasi-static and dynamic experimental results, whereas the continuous lines refer to the corresponding simulation results. Failure of the specimens are obtained at the end points of the experimental curves, as indicated by the markers. The tensile failures are generally brittle (or quasi-brittle), whereas the compressive failures are generally ductile. Note that the current simulations at the material point level do not include damage, whereby the simulation curves exceed beyond the failure points. Nevertheless, as can be seen from Figure 4, the calibrated stress vs strain curves agree reasonably well with those of the experiments, particularly for dynamic loading. Viscous effects are accounted for in both elastic and in elastoplastic ranges by the proposed model. It can be easily seen in Figure 4 that the initial stiffness increases in the elastic range and that the initial yield stress increases with increasing strain rate in compression.

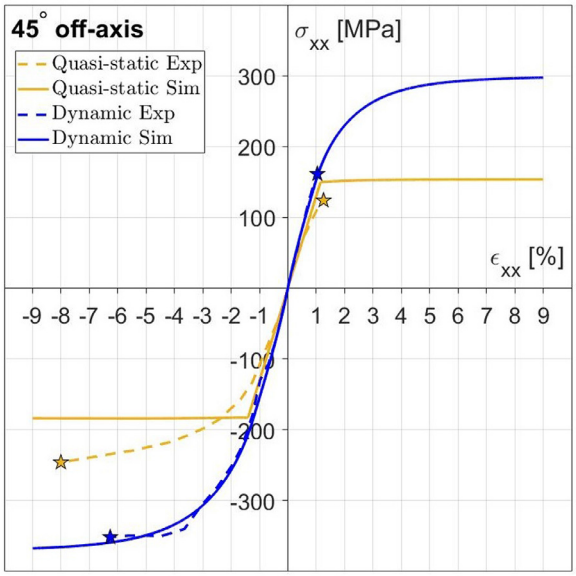

Fig. 4. Experimental response as compared to the model response after calibration of the material parameters in Table 4 for the 45° off-axis specimen. The end points of the experimental curves are indicated by star markers, signaling failure of the specimens. Both tensile and compressive loadings under quasi-static and dynamic conditions are included.

Table 4
Model parameters for the epoxy matrix material.

Calibrated			Estimated	
G_2	t_{2*}	t_*	σ_t	σ_c
GPa	s	s	MPa	MPa
1.18	1.0×10^{-5}	1.9×10^{-5}	121	180

It is worth mentioning that published strength data for pure 8552 epoxy resin is very limited. Hence, the compressive strength σ_c in the model is based on experimental data obtained by Herraez et al. (2017), leading to $\sigma_c =$ 166-198 MPa from nanoindentation tests and about $\sigma_c =$ 200 MPa from micropillar compression tests. The tensile strength σ_t value is stated by the manufacturer (Hexcel) for bulk material. It should, however, be recognised that yielding in a fibre composite occurs in very small volumes, which are related to a distance between fibres in the order of microns. There is clear evidence that the strength of such small volumes may be significantly higher than for bulk material. Hobbiebrunken et al. (2007) obtained an increase in tensile strength from about 85 MPa for bulk RTM6 epoxy to 110-170 MPa for micro-tensile specimens with a gauge volume less than 1 mm^3. A similar, size effect induced, increase in strength with decreasing volume was earlier obtained by Odom and Adams (1992) for 3501-6 epoxy.

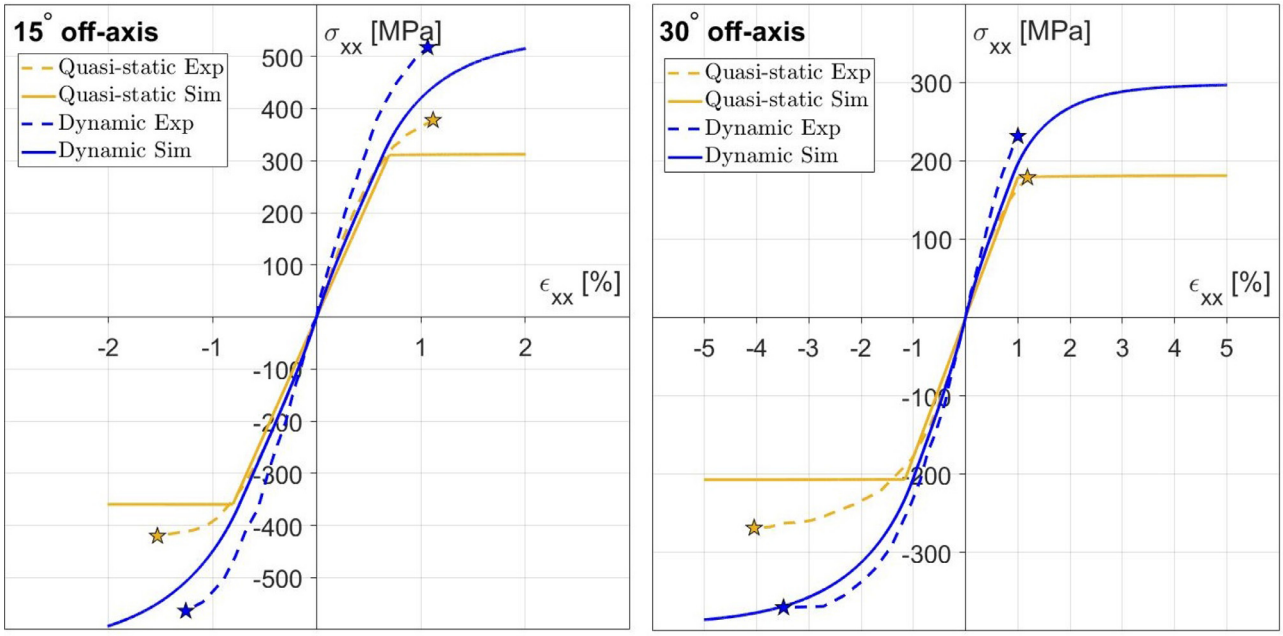

Fig. 5. Comparison between experimental data and numerical predictions for the 15 and 30° off-axis specimens in tension and compression under quasi-static and dynamic loadings. The end points of the experimental curves are indicated by markers.

Therefore, the bulk properties of the neat resin must be carefully examined before using them as input model parameters. The estimated parameters for the epoxy matrix material are shown in Table 4.

3.4. Model validation

This subsection describes validations carried out for the coupled viscoelastic-viscoplastic model response as compared to the corresponding experimental response of the IM7/8552 carbon-epoxy composite. The model parameters used in the validations are the ones from the 45° off-axis calibration in Table 4. The simulated cases are the tensile and the compressive tests with the off-axis angles: 15°, 30°, 75° and 90°. Due to lack of experimental data for the 75° off-axis specimen in tension, only the numerical predictions are presented for the 75° off-axis specimen under tensile loading. For the experimental data used in the validation, an averaging of the stress-strain data is considered based on the scatter in the experimental response in Koerber et al. (2010); Kuhn et al. (2015).

The validation results for the different off-axis angle cases are presented in Figures 5 and 6. As can be seen from the Figures, the model responses agree well with the experimental responses for the off-axis specimens in both tension and compression under dynamic loading. However, the quasi-static experimental results are less well predicted. The experimental curves under static compression deviate from linearity significantly earlier than the model response curves. We also observe an increase in stiffness for the dynamic as compared to the static model responses due the to rate sensitive viscoelastic polymer matrix constituent. In the experiment the dynamic stiffness increase is a bit higher compared to the model response for off-axis angles smaller than the 45° angle considered in the calibration, while the opposite applies to off-angles larger than the calibration angle.

A main reason for the discrepancy between the static model and experimental responses is that our adopted approach assumes a uniform stress-strain state in the polymer matrix. In reality, however, the matrix experiences a non-uniform stress-strain distribution and plastic zone development at the microscopic level. As a result, yielding initiates “earlier” in the composite corresponding to a gradual nonlinear response as compared to the simulation. Eventually, after the growth of the plastic zone, the uniform state is approached in the matrix. This is manifested by the response in Figures 4-6, where it is observed that the perfectly plastic model response catches roughly the experimental behavior. Another reason may be the relatively fast relaxation times t_{2^*} and t_2, see Table 4, leading to quasi-static elastic-perfectly plastic model response for low loading rates. With these relaxation times, the shear modulus and the apparent yield stress reach the long term values G_1, σ_c (in compression) and σ_t (in tension) in a few seconds. In addition to that, the proposed model does not consider damage in the material and the observed experimental response results from the macroscopic damage of the material. However, no experimental investigation has been performed on this material system to understand the damage mechanisms for dynamic loading. The experimental stress-strain curves under static tension of the specimens usually end prior to the onset of plasticity in the model. As a result of the triaxial tensile stress state developed in the matrix at the microscopic level, brittle failure of fibre composites under partial or pure transverse tension is well known. Such failure appears to be governed by the hydrostatic stress component, rather than by the distortional component considered in the current model, Marklund et al. (2014). In the present development dynamic compression loads are in focus, e.g. for crash applications, thus suppressing hydrostatic stress induced tensile matrix failure.

3.5. Sensitivity in model response for the off-axis angle and the fiber volume fraction

In this sub-section we focus on the sensitivity of the model response with respect to the considered off-axis angles. To complete the picture of the model behavior, the response curves in Figure 7 show the static and dynamic model responses for all the considered off-axis angles. Clearly, the largest sensitivity of the response is obtained when the off-axis angle is increased from 15 to 30°. The maximum stiffness of the ply coincides with the fibre direction and hence the stiffness increases as the fibres become more aligned with the loading direction. Likewise, the initial yield points decrease with increasing off-axis angle. Here we also note the perfectly plastic response obtained for all the static response curves. This is due to the nonlinear homogenization of the matrix/fibre response, manifesting matrix yielding combined with less significant contribution from the fibers to the composite response.

Figure 8 shows the model sensitivity to the fiber volume fraction.

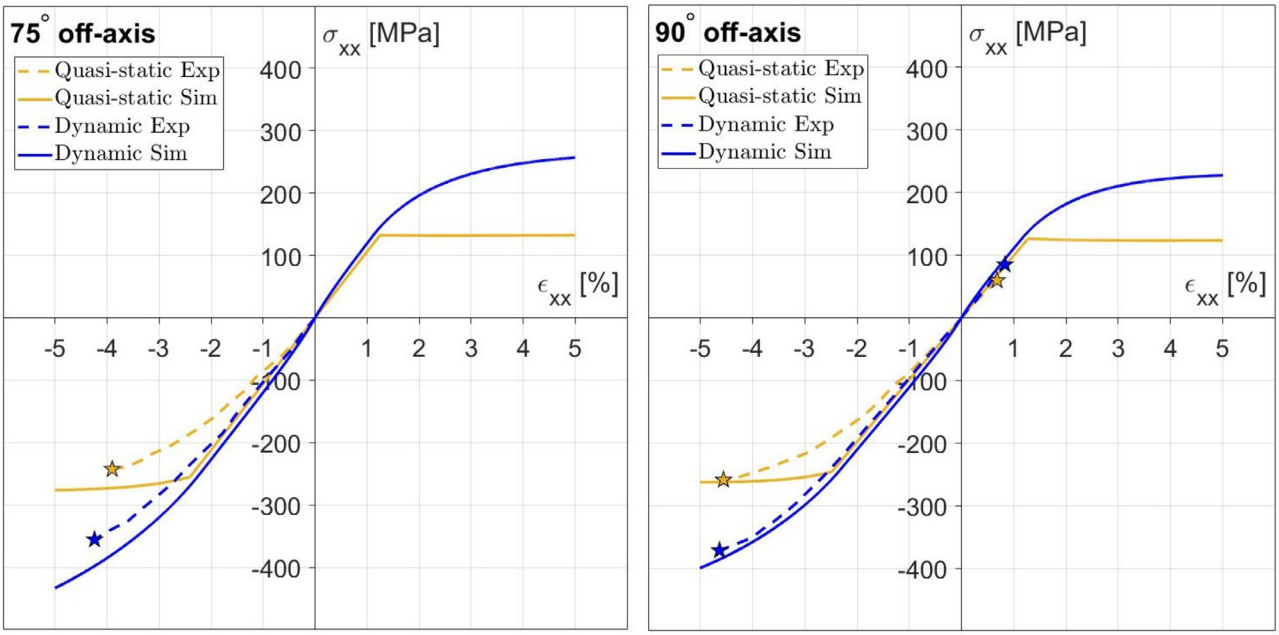

Fig. 6. Comparison between experimental data and numerical predictions for the 75 and 90° off-axis specimens in tension and compression under quasi-static and dynamic loadings. The end points of the experimental curves are indicated by markers.

The different response curves are shown for the 45° off-axis case. As expected and as shown in Figure 8, less stiff behavior is obtained for decreasing fibre volume fractions v^f, centered around the (considered) volume fraction $v^f = 57\%$.

3.6. Model prediction for neat resin behaviour

In this sub-section model predictions for the neat 8552 resin under various strain rates, ranging from quasi-static $\dot{\varepsilon} = 2.5 \times 10^{-4}$ /s up to a dynamic strain rate of $\dot{\varepsilon} = 1000$ /s are considered. For this analysis we consider the proposed viscoelastic-viscoplastic constitutive model without any carbon fibre interaction, i.e. $v^f = 0$ and $\alpha = 0$, to predict the pure resin behaviour at different strain rates. The parameters used are thus the ones in Tables 3 and 4. To this end, it is noted that most glassy amorphous polymers (including epoxy) exhibit time dependent mechanical behaviour over a wide range of strain rates. Typically, the initial part of the stress-strain curve is governed by the viscoelastic behaviour. The response then becomes nonlinear with increasing strain until the stress reaches a peak value and damage starts to develop in tension and compression. With increasing strain rates (up to very high values), these effects are manifested by increasing initial slope in the stress-strain response and increase of the apparent yield strength in the post-yield behaviour, as discussed in ref. Siviour and Jordan (2016). The reason could be that the polymer chains resist to align themselves

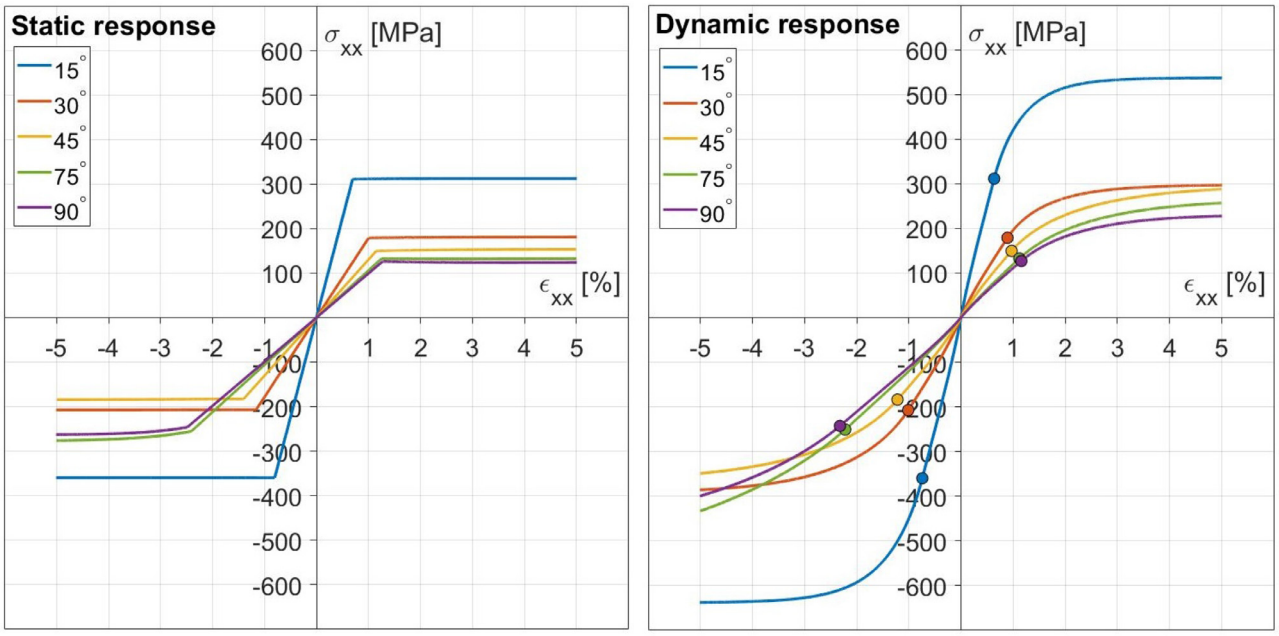

Fig. 7. Model response for specimens with different off axis angles. Both static and dynamic responses are included. The initial yield points along the dynamic response curves are marked.

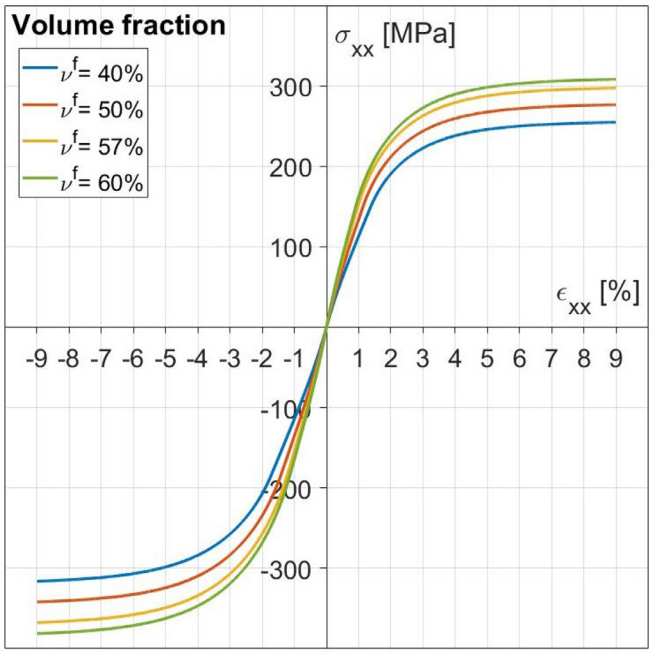

Fig. 8. Model predictions for different fiber volume fractions v^f. A specimen with the off-axis angle 45° is considered.

at high strain rates, causing a viscous strain hardening effect as proposed in Arruda et al. (1995).

The resulting model response of the neat resin from quasi-static to dynamic loadings is shown in Figure 9. In view of the expected behaviour of the polymer, it is observed that the model reasonably well predicts the rate dependent behaviour for strain rates ranging from quasi-static to dynamic loading. The viscoelastic model behaviour activates before yielding is reached and captures the increase in initial stiffness. Once the yield stress is reached the model response is thereafter governed by viscoplasticity, as evidenced by the increase in apparent yield stress in the pure resin with increasing strain rate. Also note the difference in yield stress in compression and in tension due to

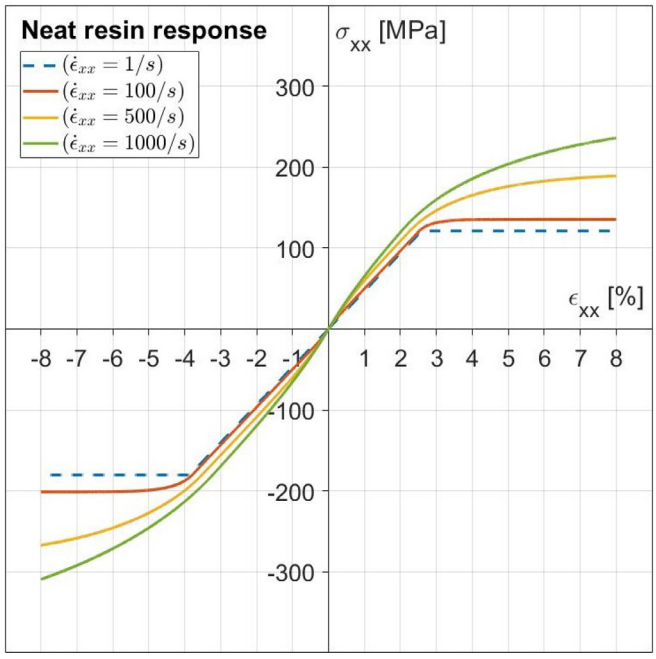

Fig. 9. Model predictions for 8552 resin under different axial strain rates.

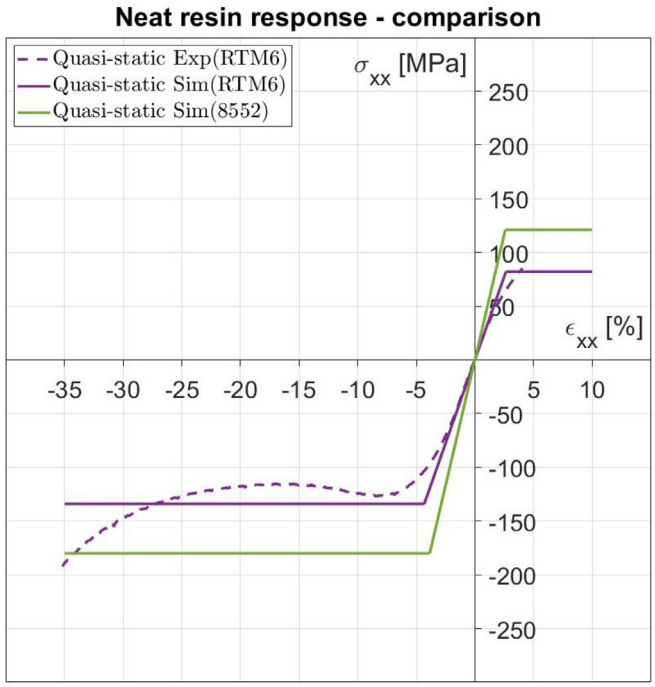

Fig. 10. Static experimental and model responses for RTM6, Marklund et al. (2014). For comparison the model response of 8552 resin is included.

the pressure sensitive yield function. As expected, for quasi-static loading, the input yield stresses σ_c = 180 MPa and σ_t = 121 MPa are captured in uniaxial compression and tension, respectively. In order to relate the model response of the 8552 resin to an epoxy with a known stress-strain curve, we have included experimental results and model prediction for an RTM6 epoxy under static tension and compression Marklund et al. (2014) in Figure 10. This Figure also includes the predicted behaviour of the 8552 epoxy.

The static model data for RTM6 are E=3.1 GPa, ν=0.38, σ_c=134 MPa and σ_t=82 MPa Marklund et al. (2014). Figure 10 illustrates the difference in static response between these resins, where the 8552 epoxy is stiffer and has higher yield stresses than the RTM6 epoxy.

4. Concluding remarks

A 3D model for capturing rate dependent response of a fiber reinforced polymer UD ply has been presented. The model is based on micromechanics with a subscale at the ply level, consisting of polymer matrix and fibre materials whose properties have a piece-wise constant distribution in the RVE. In order to describe the material behaviour of the constituents, relatively simple models are applied: confined to the matrix constituent, a rate-dependent polymer material behaviour is described by a viscoelastic-viscoplastic model. Based on the elastic isotropy of the polymer, an explicit stress update is obtained for the incremental nonlinear matrix response, which contributes to the efficiency of the total model. For the fibre material, transverse elasticity (without any inelastic response) is assumed. The constituents are connected via computational homogenization of the RVE, where the key assumptions are: 1) spatially constant straining in the fibre direction and 2) spatially constant stress in the transverse fibre plane. To handle these conditions simultaneously, a superficial strain fluctuation of the plane transverse to the fibre orientation was introduced. To facilitate the “constant stress” condition in a simplified manner, the strain fluctuation is related to the macroscopic strain via the 4th order fibre transverse operator, that projects macro-strain into the transverse fibre plane. The local equilibrium problem associated with the

homogenization is thereby manifested in terms of a projected stress balance between the fibre and the matrix constituents in the transverse fibre plane. This local projection problem is efficiently solved in terms of the local stress-strain responses of the matrix and the fibre materials.

We conclude that the homogenized material model response has been successfully verified through numerical simulations of the IM7/8552 UD composite subjected to a variety of uniaxial off-axis tests. The model response clearly reflects the strain rate dependencies in response under tensile and compressive loadings at higher strain rates focused in this paper. Since the model is micromechanical, the model assumes 11 parameters, involving both the fiber and polymer matrix constituents. However, most parameters are known from the literature, the composite system and via estimation. It turns out that only 3 of the parameters, related to the nonlinear polymer matrix behavior, need to calibrated. The simulated behaviour in Figures 4-6 is less satisfactory for quasi-static strain rates, where (fully relaxed) perfectly plastic response is obtained. The current model is, however, focused on dynamic loading situations, where the viscous effects dominate the response. Work to include the earlier initiation and subsequent growth of the yield zone without overly computationally demanding requirements is a challenging and ongoing research task. We also note that the predicted stress-strain curves extend indefinitely in the viscoplastic range, which illustrates the need to limit the nonlinear model response with a failure criterion and damage evolution. In addition, the full assessment of the specimen failure requires the consideration of the boundary value problem of the experiment, which is beyond the scope of the present paper. However, despite the relatively simple modelling assumptions for the constituents, we conclude that fairly good agreements are obtained for the homogenized response in the validation for the various off-axis tests in ref. Koerber et al. (2018).

CRediT authorship contribution statement

Larsson R.: Conceptualization, Methodology, Formal analysis, Software, Writing - original draft. **Singh V.:** Software, Investigation, Data curation, Visualization, Writing - original draft. **Olsson R.:** Validation, Investigation, Writing - review & editing, Supervision. **Marklund E.:** Validation, Investigation, Writing - review & editing.

Declaration of Competing Interest

I hereby submit the paper “A micromechanically based model for strain rate effects in unidirectional composites”. I confirm that the paper is not concurrently submitted for publication elsewhere. The paper, in its entirety, in part, or in a modified version, has not been published elsewhere.

Acknowledgement

The authors gratefully acknowledge the support of the ICONIC project under the Marie Skłodowska-Curie grant agreement No 721256 of the European Union Horizon 2020 research and innovation programme. Co-funding has also been provided from the Swedish FFI programme via VINNOVA (dnr 2016-04239) and from the development funds of RISE (RISE SICOMP SK-project 25173-1).

Integration of the matrix response using the backward Euler method

The appendix describes the backward Euler integrated response of the polymer matrix material with respect to the proposed viscoelastic-viscoplastic evolution rule. As to notation, the sub-index ”m” for the matrix material is omitted for brevity in this Appendix. From the evolution rules (31), the rate formulated constitutive relations may be written as

$$\dot{\boldsymbol{\sigma}}_d = 2G_0\dot{\boldsymbol{\epsilon}}_d - 2G_0\lambda\boldsymbol{f} - \frac{1}{t_{2*}}\boldsymbol{\sigma}_{d2} \tag{44a}$$

$$\dot{\boldsymbol{\sigma}}_{d2} = 2G_2(\dot{\boldsymbol{\epsilon}}_d^e - \dot{\boldsymbol{\epsilon}}_d^v) = 2G_2\left(\dot{\boldsymbol{\epsilon}}_d - \lambda\boldsymbol{f} - \frac{1}{2G_2 t_{2*}}\boldsymbol{\sigma}_{d2}\right) \tag{44b}$$

where the viscoplastic multiplier is $\lambda = \eta[\phi]/t_* \geq 0$.

The backward Euler integrated viscoelastic-viscoplastic flow rules follow from the sequel below; we obtain the explicit expressions for the integrated stresses $\boldsymbol{\sigma}_d$ and $\boldsymbol{\sigma}_{d2}$ in terms of their corresponding elastic trial stresses as

$$\boldsymbol{\sigma}_d = \boldsymbol{\sigma}_d^{\mathrm{tr}} - 2G_0\,\mu\boldsymbol{f} - \frac{\Delta t}{t_{2*}}\boldsymbol{\sigma}_{d2} \tag{45a}$$

$$\boldsymbol{\sigma}_{d2} = b(\boldsymbol{\sigma}_{d2}^{\mathrm{tr}} - 2G_2\,\mu\boldsymbol{f}) \tag{45b}$$

where Δt is the size of the time step and $\mu := \Delta t\lambda$ is the integrated plastic multiplier. In (45), the trial stresses are

$$\boldsymbol{\sigma}_d^{\mathrm{tr}} = {}^n\boldsymbol{\sigma}_d + 2G_0\,\Delta t\dot{\boldsymbol{\epsilon}}_d, \quad \boldsymbol{\sigma}_{d2}^{\mathrm{tr}} = {}^n\boldsymbol{\sigma}_{d2} + 2G_2\,\Delta t\dot{\boldsymbol{\epsilon}}_d \tag{46}$$

and the scalars *a, b* and c are defined as

$$a = \frac{\Delta t}{t_{2*} + \Delta t}, \quad b = \frac{t_{2*}}{t_{2*} + \Delta t}, \quad c = 1 - a\frac{G_2}{G_0} \tag{47}$$

Hence, upon combining the relations (45ab) we obtain

$$\boldsymbol{\sigma}_d = \boldsymbol{s}^{\mathrm{tr}} - 2G_0\,c\,\mu\boldsymbol{f} \tag{48}$$

where $\boldsymbol{s}^{\mathrm{tr}} := \boldsymbol{\sigma}_d^{\mathrm{tr}} - a\boldsymbol{\sigma}_{d2}^{\mathrm{tr}}$ is the deviatoric viscoelastic trial stress.

The integrated relation (48) is now immediately obtained via (31a) in terms of the radial return property

$$(\sigma_d^e + 3G_0c\mu)\frac{\boldsymbol{\sigma}_d}{\sigma_d^e} = \boldsymbol{s}^{\mathrm{tr}} = s_e^{\mathrm{tr}}\frac{\boldsymbol{s}^{\mathrm{tr}}}{s_e^{\mathrm{tr}}} \text{ with } s_e^{\mathrm{tr}} = \sqrt{\frac{3}{2}}|\boldsymbol{s}^{\mathrm{tr}}: \boldsymbol{s}^{\mathrm{tr}}| \tag{49}$$

whereby it follows that

$$\sigma_d^e = s_e^{\mathrm{tr}} - 3G_0c\mu \text{ and } \boldsymbol{f} = \boldsymbol{f}^{\mathrm{tr}} = \frac{3}{2}\frac{\boldsymbol{\sigma}_d}{\sigma_d^e} = \frac{3}{2}\frac{\boldsymbol{s}^{\mathrm{tr}}}{s_e^{\mathrm{tr}}} \tag{50}$$

Upon inserting this relation into the integrated viscoplastic multiplier for the Bingham model we obtain

$$\mu = \begin{cases} \dfrac{\Delta t}{c\Delta t + t_*}\dfrac{\phi^{\mathrm{tr}}}{3G_0} & \phi^{\mathrm{tr}} > 0 \\ 0 & \phi^{\mathrm{tr}} \le 0 \end{cases} \tag{51}$$

where $\phi^{\mathrm{tr}} = s_e^{\mathrm{tr}} - (c_y + \gamma p)$ and $p = -K\epsilon_{vol}$. It may be noted that for the Bingham model an explicit expression for the integrated viscoplastic multiplier μ is obtained.

References

Arruda, E.M., Boyce, M.C., Jayachandran, R., 1995. Effects of strain rate, temperature and thermomechanical coupling on the finite strain deformation of glassy polymers. Mechanics of Materials 19 (2), 193–212.

Carruthers, J.J., Kettle, A.P., Robinson, A.M., 1998. Energy absorption capability and crashworthiness of composite material structures : A review. Applied Mechanics Reviews 51 (10), 635–649.

Christensen, R., Lo, K.H., 1979. Solutions for effective shear properties in three phase sphere and cylinder models. Journal of the Mechanics and Physics of Solids 27, 315–330.

Daniel, I.M., Liber, T., 1976. Strain rate effects on mechanical properties of fiber composites, part 3. Technical Report NASA-CR-135087. IIT Research Institute, Chicago, USA.

Fiedler, B., Hojo, M., Ochiai, S., Schulte, K., Ando, M., 2001. Failure behavior of an epoxy matrix under different kinds of static loading. Composites Science and Technology 61, 1615–1624.

Gerbaud, P.-W., Otero, F., Bussetta, P., Camanho, P., 2019. An invariant based transversely-isotropic constitutive model for unidirectional fibre reinforced composites considering the matrix viscous effects. Mechanics of Materials 138 (doi: 10.1016/j.mechmat.2019.103146).

Grauers, L., Olsson, R., Gutkin, R., 2014. Energy absorption and damage mechanisms in progressive crushing of corrugated NCF laminates: Fractographic analysis. Composite Structures 110, 110–117.

Hashin, Z., 1983. Analysis of composite materials - a survey. Journal of Applied Mechanics 50, 481–505.

Herraez, M., Naya, F., Gonzalez, C., Monclus, M., Molina, J., Lopes, C.S., LLorca, J., 2017. Microscale characterization techniques of fibre-reinforced polymers. Springer. chapter 10

Hexcel Corporation, 2020a. Hexply 8552 product data sheet. EU version.

Hexcel Corporation, 2020b. Hextow IM7 carbon fiber datasheet. Global version.

Hill, R., 1963. Elastic properties of reinforced solids: Some theoretical principles. Journal of the Mechanics and Physics of Solids 11, 357–372.

Hobbiebrunken, T., Fiedler, B., Hojo, M., Tanaka, M., 2007. Experimental determination of the true epoxy resin strength using micro-scaled specimens. Composites Part A: Applied Science and Manufacturing 38 (3), 814–818.

Hosur, M.V., Alexander, J., Vaidya, U.K., Jeelani, S., 2001. High strain rate compression response of carbon/epoxy laminate composites. Composite Structures 52 (3-4), 405–417.

Hsiao, H.M., Daniel, I.M., 1998. Strain rate behavior of composite materials. Composites Part B: Engineering 29 (5), 521–533.

Hsiao, H.M., Daniel, I.M., Cordes, R.D., 1999. Strain rate effects on the transverse compressive and shear behaviour of unidirectional composites. Journal of Composite Materials 33 (17), 1620–1642.

Jacob, G.C., Fellers, J.F., Simunovic, S., Starbuck, J.M., 2002. Energy absorption in polymer composites for automotive crashworthiness. Journal of Composite Materials 36 (7), 813–850.

Koerber, H., Kuhn, P., Ploeckl, M., Oterio, F., Gerbaud, P.-W., Rolfes, R., Camanho, P.P., 2018. Experimental characterization and constitutive modelling of the non-linear stress-strain behaviour of unidirectional carbon-epoxy under high strain rate loading. Advanced Modeling and Simulation in Engineering Sciences 5 (17).

Koerber, H., Xavier, J., Camanho, P., 2010. High strain rate characterisation of unidirectional carbon-epoxy IM7/8552 in transverse compression and in-plane shear using digital image correlation. Mechanics of Materials 42 (11), 1004–1019.

Kuhn, P., Ploeckl, M., Koerber, H., 2015. Experimental investigation of the failure envelope of unidirectional carbon-epoxy composite under high strain rate transverse and off-axis tensile loading. EPJ Web of Conferences 94 (01040). Doi: 10.1051/epjconf/20159401040

Larsson, R., Gutkin, R., Rouhi, S., 2018. Damage growth and strain localization in compressive loaded fiber reinforced composites. Mechanics of Materials 127, 77–90.

Marklund, E., Asp, L., Olsson, R., 2014. Transverse strength of unidirectional non-crimp fabric composites: Multiscale modelling. Composites Part B 65, 47–56.

Miehe, C., Schroder, J., Schotte, J., 1999. Computational homogenization analysis in finite plasticity. Simulation of texture development in poly- crystalline materials. Computer Methods in Applied Mechanics and Engineering 171, 387–418.

Mori, T., Tanaka, K., 1973. Average stress in matrix and average elastic energy of materials with misfitting inclusions. Acta Materialia 21, 571–574.

Mårtensson, P., 2016. Framework of cost and weight efficient conceptual design of automotive composite body structures. KTH Royal Institute of Technology Ph.D. thesis.

Odom, E.M., Adams, D.F., 1992. Specimen size effect during tensile testing of an unreinforced polymer. Journal of Materials Science 27 (7), 1767–1771.

Ponte Castañeda, P., 1996. Exact second-order estimates for effective mechanical properties of nonlinear composite materials. Journal of the Mechanics and Physics of Solids 44, 827–862.

Sierakowski, R.L., 1997. Strain rate effects in composites. Applied Mechanics Reviews 50 (12), 741–761.

Singh, V., 2018. Literature survey of strain rate effects on composites. TR18-001, Swerea SICOMP, Mölndal

Siviour, C.R., Jordan, J.L., 2016. High strain rate mechanics of polymers: A review. Journal of Dynamic Behavior of Materials 2 (1), 15–32.

Steinmann, P., Larsson, R., Runesson, K., 1997. On the localization properties of multiplicative hyper elasto-plastic continua with strong discontinuities. International journal of solids and structures 34, 969–990.

Suquet, P., 1985. Local and global aspects in the mathematical theory of plasticity. Elsevier Applied Science Publishers, London.

Van Ee, D., Poursartip, A., 2009. HexPly 8552 Material Properties Database for use with COMPRO CCA and RAVEN. http://www.niar.wichita.edu/coe/ncamp.asp. NCAMP, Wichita, KS.

Vogler, M., Rolfes, R., Camanho, P., 2013. Modeling the inelastic deformation and fracture of polymer composites - Part I: Plasticity model. Mechanics of Materials 59, 50–64.

Yokoyama, T., Nakai, K., 2009. Impact compressive failure of a unidirectional carbon/epoxy laminated composite in three principal material directions.